

Solid immersion lens-enhanced nano-photoluminescence: Principle and applications

S. Moehl, Hui Zhao,^{a)} B. Dal Don, S. Wachter, and H. Kalt
*Institut für Angewandte Physik and Center for Functional Nanostructures,
Universität Karlsruhe (TH), D-76131 Karlsruhe, Germany*

(Received 10 October 2002; accepted 21 February 2003)

We demonstrate a far-field nano-photoluminescence setup based on the combination of a hemispherical solid immersion lens (SIL) with a confocal microscope. The spatial resolution is confirmed to be 0.4 times the wavelength in vacuum in terms of half width at half maximum. The collection efficiency is found to be about five times higher than the same microscope without SIL, which is consistent with our theoretical analysis. We investigate in detail the influence of an air gap between the SIL and the sample surface on the system performance, and prove both experimentally and theoretically the tolerance of this far-field system to an air gap of several micrometers. These features make the present setup an ideal system for spatially resolved spectroscopy of semiconductor nanostructures. In particular, we show two examples of such applications in which the present setup is clearly suitable: Studies of excitonic transport in quantum wells and spectroscopy of single quantum dots with emphasis on polarization dependence and weak-signal detection. © 2003 American Institute of Physics. [DOI: 10.1063/1.1567035]

I. INTRODUCTION

Photoluminescence (PL) is one of the most important methods used to investigate electronic states in semiconductors. Since semiconductor nanostructures are becoming increasingly important in optoelectronic applications, PL has been developed into a local spectroscopy method. To realize a spatial resolution of 1 μm or less, one needs local excitation, local detection, or both. In far-field optics, the resolution is limited by diffraction. In a common microphotoluminescence ($\mu\text{-PL}$) system, the achieved resolution is about 1 μm (for a review, see Ref. 1). This limitation of the resolution can be overcome by working in the near-field regime, where the diffraction limit is not yet established. Scanning near-field optical microscopy (SNOM), designed according to this idea, realizes a resolution of less than 100 nm. Within the far-field regime, the diffraction limitation can be dealt with by increasing the refractive index of the media around the sample, i.e., increasing the effective numerical aperture (NA_{eff}) of the optical system. This can be realized by immersing the sample into oil or by putting a tiny lens, namely a solid immersion lens (SIL), on the surface of the sample. In the case of semiconductor spectroscopy, the latter is more suitable since a SIL is easily dealt with, and there is no risk of contaminating sample. Also, with a SIL, the experiments can be performed at low sample temperature.

During the last decade, SILs have been used in solid immersion microscopes² and (magneto-)optical data storage³ for high spatial resolution or high storage density, respectively. Recently, SIL has also been introduced in spatially resolved pump-probe experiments.^{4,5} By including a super-spherical SIL⁶ (s-SIL) in a microscope system, an improved

spatial resolution at room temperature⁷ as well as low temperatures⁸ have been demonstrated by PL-imaging measurements of GaAs quantum wells (QWs). The high spatial resolution has enabled the study of carrier migration under global⁸ or local⁹ excitation conditions. The s-SIL has also been used in a spatially resolved PL setup to investigate exciton localization in GaAs QWs.^{10,11}

Up to now, s-SILs have generally been applied in PL systems. We note, however, that the thickness of an s-SIL is designed for one particular wavelength since the incident parallel beam to the objective is focused at the distance $r(1 + 1/n_{\text{SIL}})$ away from the top of the s-SIL, where r is the radius of the SIL and n_{SIL} is the refractive index of the SIL material. Consequently, the focus of an s-SIL is wavelength dependent since n_{SIL} depends on the wavelength of light, λ . In contrast, a hemispherical SIL (h-SIL) is universal for any wavelength. In a PL experiment, one typically deals with different wavelengths for excitation and detection. Thus, although an s-SIL can improve the resolution n_{SIL}^2 times while an h-SIL can only improve it n_{SIL} times, the latter is more appropriate for PL studies.

In this article, we demonstrate the combination of an h-SIL with a confocal microscope. We confirm the realization of a nano-PL setup with a spatial resolution of 0.4λ by introducing the h-SIL. An enhancement of collection efficiency by a factor of 5 is found, which is consistent with a theoretical estimate. We discuss in detail the influences of an air gap between the SIL and the sample surface on the resolution and collection efficiency. We demonstrate that an air gap of several micrometers can be tolerated in a system with $\text{NA}_{\text{eff}} < 1$. Finally, some applications of this system to semiconductor spectroscopy are discussed, and a comparison with the performance of SNOM is made.

^{a)} Author to whom correspondence should be addressed; electronic mail: hui.zhao@ee.tamu.edu

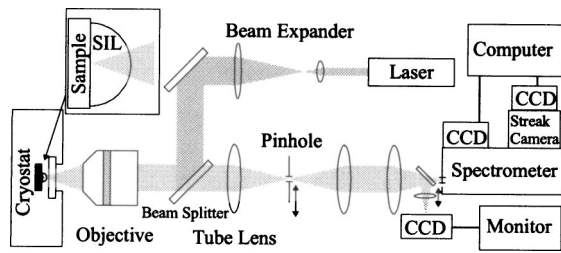


FIG. 1. Experimental setup of the SIL-enhanced nano-PL. The inset shows the SIL-sample configuration.

II. SYSTEM CHARACTERIZATION

A. Experimental setup

Figure 1 shows schematically the SIL-enhanced nano-PL system. The excitation source can be a continuous wave (cw) or pulsed laser. The laser beam is expanded to fit the diameter of objective, then reflected by a beam splitter and focused on the sample surface through a microscope objective (magnification $20\times$, numerical aperture $NA_{\text{obj}}=0.4$). The same objective is used for collecting the PL from the sample. The PL single is passed by the beam splitter and is focused by a tube lens onto the image plane of the microscope. A set of pinholes with different sizes is installed in the image plane to select the detection area. By scanning the pinhole in the image plane, one can detect luminescence from different positions on the sample surface. This also allows one to separately move the detection and excitation spots. A movable assembly consisting of a mirror and a lens is installed in front of the spectrometer, to provide the option of reflecting and focusing the light onto a charge coupled device (CCD) camera connected to a monitor. This configuration achieves direct imaging of the sample surface on the monitor, thus facilitating fine alignments of the sample, the SIL, the objective, and the pinhole. Also, by removing the pinhole, one can take PL intensity maps by exciting the sample globally. When the mirror is shifted out of the optical path, the signal is sent into the spectrometer having a spectral resolution of $30 \mu\text{eV}$. For cw measurements, the PL is recorded by a cooled CCD camera. For time-resolved measurements, a streak camera with a temporal resolution of 2 ps is used in combination with a CCD camera in the photon-counting mode.

The h-SIL made of ZrO_2 with $n_{\text{SIL}}=2.16$ at $\lambda=600 \text{ nm}$ is adhesively fixed to the sample surface. The sample with the SIL is vertically mounted in a helium-flow cryostat. The SIL can be used in the temperature range of 6–300 K for an unlimited number of cooling cycles. The diameter of the SIL is chosen to be 1 mm, which is large enough to give a sufficiently large working area for imaging spectroscopy and to allow handling without any special equipment, but is still small enough to be stuck on the sample adhesively even in the vertical configuration.

B. Spatial resolution

In a far-field optical system, the spatial resolution is limited by diffraction of the light. For an incident plane light wave, the half width at half maximum (HWHM) of the Airy pattern is given by

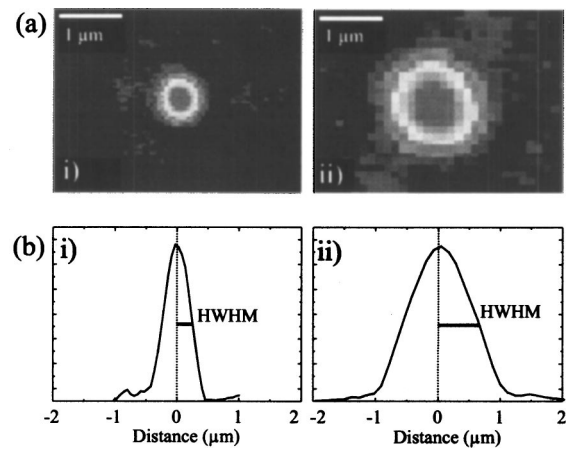


FIG. 2. Intensity maps (a) and cross sections (b) of the focused laser spot on an arbitrary sample. The width of the spot obtained with SIL (i) is n_{SIL} times narrower than that without SIL (ii).

$$\text{HWHM} = \frac{0.26\lambda}{nNA_{\text{obj}}}. \quad (1)$$

Here, n represents the refractive index of the media around the sample. Without SIL, $n \approx 1$ (air) and with the h-SIL we have $n = n_{\text{SIL}} = 2.16$. Thus, by introducing the h-SIL we can improve the resolution by a factor of 2 in diameter, thus a factor of 4 in spot area. In order to confirm the enhanced resolution, we install the SIL onto a sample having a flat surface and focus the incident laser beam from a He–Ne laser onto the sample surface (i) through or (ii) bypassing the SIL, respectively. We then measure two-dimensional intensity maps of the laser spots in both cases, as shown in Fig. 2(a) with the same gray scale encoding. The length-scale calibration in these maps is obtained by imaging an optical grating with known parameters. The spatial intensity profiles in Fig. 2(b) are obtained by taking a line scan across the laser spots. As expected, the profile with the SIL (i) is about two times narrower than that obtained without the SIL (ii). In (i) the realized spatial resolution (HWHM of the laser spot) is 0.4λ [corresponding to 260 nm for the He–Ne laser (633 nm)] in contrast to 0.8λ for (ii). We note that the achieved values of HWHM in both cases are larger than that calculated from Eq. (1). This is consistent with theoretical estimates,¹² and can be attributed to the Gaussian profile of the laser beam used in the experiment, as opposed to a plane wave,¹³ and the high NA of the system.¹²

In a confocal microscope system, the resolution can be further improved by introducing a pinhole of a suitable size to the image plane of the microscope.¹³ In the following, we present a quantitative analysis of this further improvement. The illumination function of the laser excitation can be described by a Gaussian function

$$i_{\text{ill}}(q) = \exp\left(-2 \frac{q^2}{w_{\text{laser}}^2}\right). \quad (2)$$

Here, q is the coordinate in the focal plane, i.e., sample surface, and w_{laser} is the spot radius at $1/e^2$. The detection function i_{det} can also be described by a Gaussian function, but with a different radius w_{lumi} since generally the wavelength

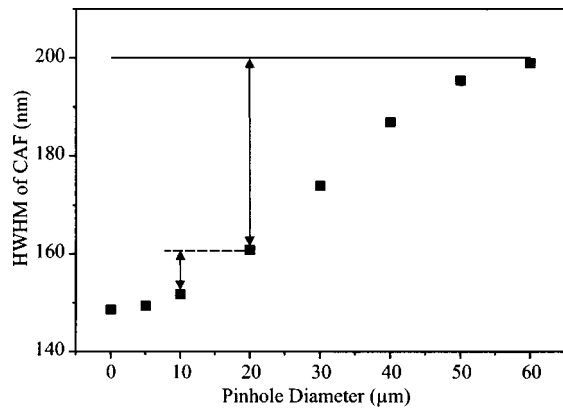


FIG. 3. Calculated HWHM of the confocal acceptance function (CAF) as function of the pinhole diameter. The horizontal line represents the HWHM obtained with an infinitely large pinhole. In the calculation, the excitation and detection wavelengths are 476.5 and 529 nm, respectively, which are consistent with the experimental conditions.

of the luminescence is different from that of the excitation laser in a PL experiment. The transmission function of the pinhole is

$$t_p(q) = \text{rect}\left(\frac{q}{q_0}\right) = \begin{cases} 1 & |q| < q_0 \\ 0 & |q| > q_0 \end{cases} \quad (3)$$

with q_0 the radius of the pinhole image. Thus, the detection probability, i.e., the probability that a photon emitted at point p will be transmitted through the pinhole, and thus detected, is given by

$$\begin{aligned} c(q) &= t_p(q) * i_{\text{det}}(q) \\ &= \int_0^{q_0} q' dq' \int_0^{2\pi} d\Phi' \\ &\quad \times \exp\left(-2 \frac{q^2 - 2qq' \cos \Phi' + q'^2}{w_{\text{det}}^2}\right). \end{aligned} \quad (4)$$

The confocal acceptance function (CAF) is then given by

$$p_{\text{conf}}(q) = i_{\text{ill}}(q) \cdot c(q). \quad (5)$$

Based on the above analysis, we calculate p_{conf} of our SIL-enhanced nano-PL system. Figure 3 shows the calculated HWHM of the CAF, which defines the confocal resolution, as function of the pinhole size. The horizontal line represents the resolution obtained without a pinhole. We find that a pinhole of 60 μm has no effect on the resolution, but decreasing the pinhole size below that value enhances the resolution. Below 10 μm , the enhancement is saturated.

In order to confirm that the enhancement of resolution by the SIL and pinhole can be achieved in a realistic PL measurement, we measure the spectra from a ZnCdSe/ZnSe quantum-dot sample with different SIL-pinhole configurations. In this sample, a ZnCdSe layer with a thickness of 2.9 ML is embedded between two ZnSe barriers, including Cd-rich quantum dots with an average size of about 10 nm. Excitonic transitions in individual dots lead to sharp lines observed in PL spectrum. The variations in size, shape and composition of these dots result in a wide spectral distribution of the lines. Hence, in a macroscopic PL spectrum (not

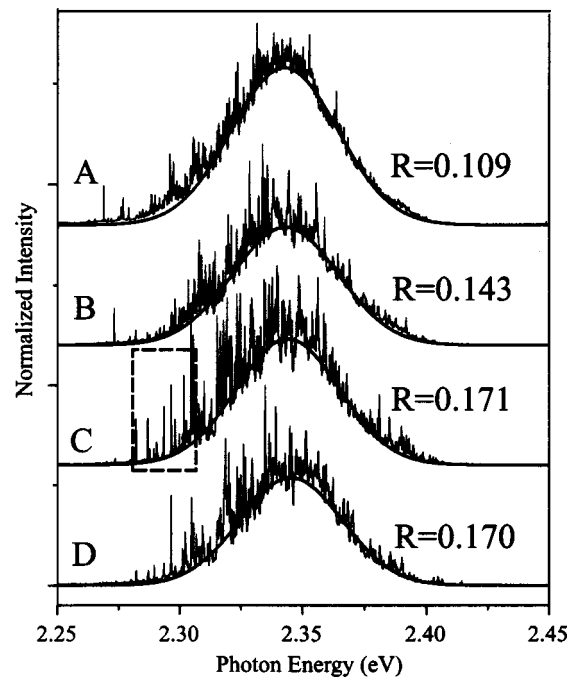


FIG. 4. PL spectra of a ZnCdSe/ZnSe quantum-dot sample measured with different configurations. A: without SIL and pinhole; B: with SIL but without pinhole; C: with SIL and 20 μm pinhole; D: with SIL and 10 μm pinhole. The low-energy side of curve C within the dashed box is also shown in Fig. 9(b) expanded to better show the sharp lines.

shown here) one observes a broad smooth emission band due to the large number of contributing dots. When the detection area, and hence the number of the dots, is decreased, individual sharp lines can be resolved on top of the unresolved smooth background. The resolved part becomes more and more pronounced with decreasing detection area. Such a sample with a rather large dot density can be used to prove qualitatively the enhancement of spatial resolution by introducing the SIL.

Figure 4 shows four spectra detected at a sample temperature of 6 K with different SIL-pinhole configurations, i.e., without SIL and pinhole (A), with SIL but without pinhole (B), with SIL and a pinhole of 20 μm diameter (C), with SIL and a pinhole of 10 μm diameter, respectively. The sample is excited by the 476.5 nm line of an Ar-ion laser. All spectra are composed of a resolved and an unresolved part, but the resolved sharp lines in the spectrum are more pronounced as we go from (A) to (D). We fit the background by a Gaussian function in order to separate the resolved and the unresolved part. The choice of a Gaussian is legitimate because of the inhomogeneous distribution of the large number of quantum dots contributing to the spectra. For each spectrum, we calculate the ratio, R , of the spectrally integrated intensities of the resolved part to the unresolved smooth background. This ratio increases with enhanced resolution of the system, as we discussed above. From Fig. 4 we obtain an increase of R by 30% by introducing the SIL [compare 0.109 for (A) to 0.143 for (B)]. By introducing a 20 μm pinhole, R is further increased by 20% [0.171 for (C)]. In case D, a 10 μm pinhole is used. But we do not find a further increase of R [0.170 for (D)]. This is consistent with our analysis dis-

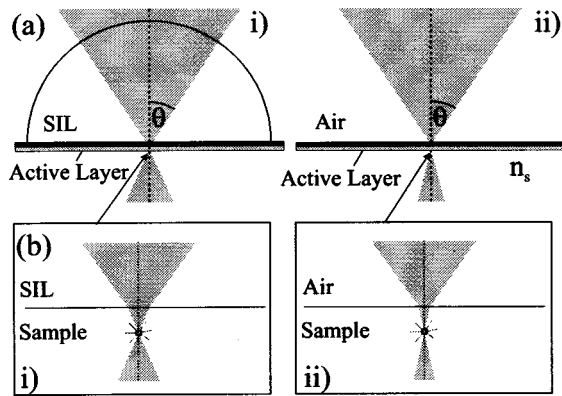


FIG. 5. Schematic drawing of the SIL-sample configuration. The enhancement of collection efficiency is explained by higher transmission (a) and a larger collection angle in the sample (b).

cussed above. As shown in Fig. 3, the enhancement of the resolution introduced by changing from a $20\ \mu\text{m}$ pinhole to a $10\ \mu\text{m}$ one is much smaller than that introduced going from no pinhole to a $20\ \mu\text{m}$ pinhole (vertical lines). In practice, the signal level drops seriously as the pinhole size is decreased below $20\ \mu\text{m}$, and the alignment becomes more difficult. Thus, a pinhole size of $20\ \mu\text{m}$ is the optimal choice in our system. With this configuration, individual sharp lines can be resolved even for this kind of sample which has a rather high dot density. [See the low-energy side of curve C in Fig. 4, Fig. 9(b) for a close-up, and discussions below.]

C. Collection efficiency

In a PL experiment, only part of the luminescence from the sample can be collected due to the reflection losses and the finite size of the optics. The collection efficiency of a spectroscopy system is of crucial importance, especially in the cases of low intensity excitation or low signal level. Generally, SNOM experiments with a high spatial resolution yield a rather low collection efficiency. By using an uncoated tip, the collection efficiency can be significantly improved, but simultaneously the spatial resolution is limited to about $200\ \text{nm}$.¹⁴ In contrast, $\mu\text{-PL}$ is operated in the far-field regime, and thus has a high collection efficiency. By introducing a SIL into a $\mu\text{-PL}$ system, the collection efficiency can be further improved.^{15–18} By comparing the luminescence intensities measured with SIL and without SIL, we find the enhancement of collection efficiency of our system using the SIL is about five times. Small variations of this factor, typically less than 20%, depend mainly on the cleaning process of both the sample and the SIL.

Here, we present a quantitative analysis of the enhancement of the collection efficiency introduced by using the SIL. Since the n_{SIL} is smaller than the refractive index of the sample, n_{samp} , but larger than that of air, the SIL has the property of reducing the reflection losses, i.e., to enhance the transmission of both the luminescence and the laser. The enhancement of the collection efficiency by this factor, k_T , can be calculated by using the Fresnel formula. Figure 5(a) shows the configurations used for our calculation of k_T by comparing the transmissions when the SIL is used (i) or not

(ii). In case (i), since the light enters perpendicular to the top surface of the SIL, the intensity transmission coefficient from air to the SIL is given by $4n_{\text{SIL}}/(1+n_{\text{SIL}})^2$ for all rays. However, when entering the sample, the transmission coefficient depends on the angle of incidence and the polarization of the ray. This angle dependency is weak in the range of angles given by our microscope objective. Thus, for simplicity, we calculate for each polarization the transmission of a ray with an angle of $\theta/2$ to the optical axes. Furthermore, the transmissions of s and p polarizations are averaged to get the total transmission. Considering the reflection losses of both the laser and the luminescence, we get an enhancement factor $k_T=1.2$.

But more important than this transmission enhancement, the SIL can enlarge the collection angle of the $\mu\text{-PL}$ system, as shown in Fig. 5(b). The solid angle outside of the sample is independent of whether the SIL is used (i) or not (ii) and is directly given by NA_{obj} . However, the solid angle inside the sample increases when the SIL is introduced. This is due to the smaller refraction of light at the sample surface since the material on top of the sample now has a refractive index higher than that of air. As a result, a point source emitting light in all directions as shown in Fig. 5(b) experiences a larger solid angle in which the emitted photons can be collected by the objective. A ray emitted outside of this angle will miss the objective and not contribute to the signal, even if its angle to the optical axis is smaller than the critical angle of total internal reflection. In the approximation that the photons are emitted from the point source homogeneously in all directions, the enhancement of collection efficiency due to the larger PL collection angle, k_Ω , is given by the ratio of the solid angles

$$k_\Omega = \frac{\Omega_{\text{SIL}}}{\Omega_{\text{air}}} \approx \frac{1 - \cos\left(\frac{n_{\text{SIL}}}{n_{\text{samp}}} \sin \theta\right)}{1 - \cos\left(\frac{1}{n_{\text{samp}}} \sin \theta\right)} \approx \frac{1 - \left(1 - \frac{1}{2} \left(\frac{n_{\text{SIL}}}{n_{\text{samp}}}\right)^2 \sin^2 \theta\right)}{1 - \left(1 - \frac{1}{2} \left(\frac{1}{n_{\text{samp}}}\right)^2 \sin^2 \theta\right)} = n_{\text{SIL}}^2. \quad (6)$$

Thus, the total enhancement of the collection efficiency by SIL is simply

$$k_{\text{total}} = k_T \cdot k_\Omega \approx k_T \cdot n_{\text{SIL}}^2. \quad (7)$$

In our setup, we have $k_T=1.2$, $k_\Omega=4.8$ so $k_{\text{total}}=5.76$. This calculated value is consistent with our experimental results.

III. INFLUENCE OF AN AIR GAP

In the analyses of the previous section, we assume that the SIL is ideally attached to the sample surface. In a realistic experiment, there exists an air gap between the flat surface of the SIL and the sample surface due to the fluctuations of both surfaces as well as due to particles between them. In this section, we discuss the influence of such an air gap on the resolution and collection efficiency of the SIL-enhanced nano-PL system.

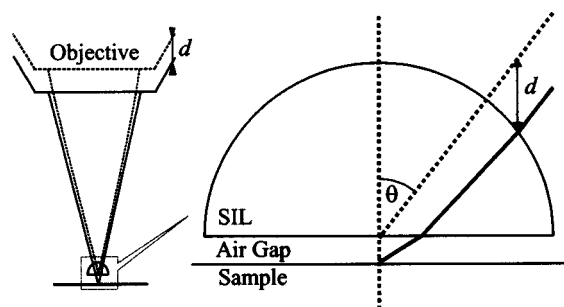


FIG. 6. Left: Schematic drawing of the objective-SIL-sample configuration when the laser beam is focused to the sample surface (solid line) and the flat surface of the SIL (dotted line); Right: Details near the sample surface. The angle θ is defined by the NA of the objective.

As discussed above, the NA_{eff} of a SIL-enhanced nano-PL system is determined by the NA_{obj} and n_{SIL} , i.e., $NA_{\text{obj}} \cdot n_{\text{SIL}}$ for an h-SIL and $NA_{\text{obj}} \cdot n_{\text{SIL}}^2$ for an s-SIL. The influence of the air gap on the resolution depends strongly on whether $NA_{\text{eff}} > 1$ or not. In a system with $NA_{\text{eff}} > 1$, a description in the near-field regime is required. Theoretical analysis shows that even an air gap with a thickness of one fifth of the wavelength can deteriorate the resolution seriously.¹⁹ In contrast, a system with $NA_{\text{eff}} < 1$ is still in the far-field regime, and it has been shown theoretically that an air gap of several micrometers does not influence the resolution.²⁰ In our setup, we have $NA_{\text{eff}} = 0.864 < 1$ and thus far-field coupling. To check the influence of an air gap on the resolution of our system, we load the SIL on the sample with and without the cleaning procedure, respectively. In the latter case, an air gap of several micrometers is anticipated (we will prove this fact later). We focus the laser beam onto the sample surface, and in both cases we get the same size for the laser spots. Thus we confirm that in a system with $NA_{\text{eff}} < 1$, an air gap of several micrometers has no influence on the resolution.

Generally, an air gap introduces additional reflection losses between the sample and the SIL, thus reduces the collection efficiency. In the near-field regime with $NA_{\text{eff}} > 1$, the collection efficiency can be deteriorated seriously by an air gap of several hundreds nanometers, i.e., comparable to the light wavelength.²⁰ In contrast, a system with $NA_{\text{eff}} < 1$ is anticipated to be more robust due to the far-field conditions. In order to investigate the tolerance of our system to the air gap, we load the SIL onto a ZnCdSe/ZnSe quantum-dot sample without any cleaning procedure. By comparing the spectra measured beneath or next to the SIL at a sample temperature of 6 K, we find an *enhancement* of the collection efficiency by a factor of 2.

To explain the observed enhancement, we calculate the collection efficiency of the system with an air gap. Figure 6 shows the configuration of the objective, SIL, air gap, and the sample. In the measurement we focus onto the sample surface. The ray-path is shown as the solid lines in Fig. 6. The dotted lines show the situation when the laser beam is focused on the flat surface of the SIL. Using the monitor CCD (Fig. 1) we can clearly observe the images of both surfaces, thus accurately measure the difference between the two focal planes, d . In this experiment, we have d

$= 40 \mu\text{m}$. By some simple geometrical considerations, we deduce the thickness of the air gap to be $5 \mu\text{m}$ from the measured d . Based on Fig. 6, we calculate the collection efficiency of this configuration by the method discussed in the previous section. We obtain $k_T = 0.55$ and $k_\Omega = 4.27$ so that $k_{\text{total}} = 2.36$. The calculation is consistent with the experiment. We note that the deterioration of enhancement from 5.76 to 2.36 by the $5 \mu\text{m}$ air gap originates mainly from the increase of the reflection losses (k_T drops from 1.2 to 0.55). The enhancement due to the enlarged collection angle, k_Ω , is not sensitive to the presence of the air gap.

In summary, we prove the tolerance of the SIL-enhanced nano-PL system to an air gap of several micrometers. In a typical measurement, there exists an air gap of about $1 \mu\text{m}$ between the SIL and the sample surface after a regular cleaning procedure. The enhancement factor of the collection efficiency is then about 5 in our experiments, as mentioned above. In principle, by increasing the NA_{obj} or n_{SIL} , or using an s-SIL, one can further improve the resolution of a SIL-enhanced nano-PL system. But, if the NA_{eff} is increased beyond one, the near-field regime is reached, and the tolerance to the air gap drops seriously. In this sense, our choice of $NA_{\text{eff}} = 0.864$ is a good compromise between the enhancement of spatial resolution and collection efficiency as well as the feasibility in practical operations. Still, it is worth noting that the described configuration can be used even for samples having rough surfaces with fluctuations of several micrometers.

IV. APPLICATIONS

Generally, the SIL-enhanced nano-PL system described above can be applied to any semiconductor spectroscopy experiment whenever the spatial resolution is needed and the sample has a relative flat surface. In some cases, this system is particularly suitable. We present in the following two kinds of applications where the SIL-enhanced nano-PL system shows its unique advantages.

A. Exciton transport in quantum wells

The exciton in-plane transport process is an important part of exciton dynamics in QWs. Due to the continuing miniaturization of electronic and optical devices thus the increasing importance of nanostructures, transport has to be understood on a length scale comparable to the light wavelength. The resolution of a conventional $\mu\text{-PL}$ system (about $1 \mu\text{m}$) is not enough for these kinds of studies. In SNOM, one can achieve a resolution of less than 100 nm by using a coated tip. But the collection efficiency is poor. Furthermore, a SNOM experiment has another disadvantage for transport measurement: One cannot detect spatially resolved spectra from positions outside the excitation spot. Thus, one can only study the transport process indirectly.

In contrast, the SIL-enhanced nano-PL can be used to investigate the transport behavior in a rather direct way with sub μm resolution. By scanning the pinhole in the image plane of the microscope, one can detect luminescence from positions which are different from the position where the sample is locally excited. This enables one, e.g., to get the spatial profile of the luminescence intensity which is related

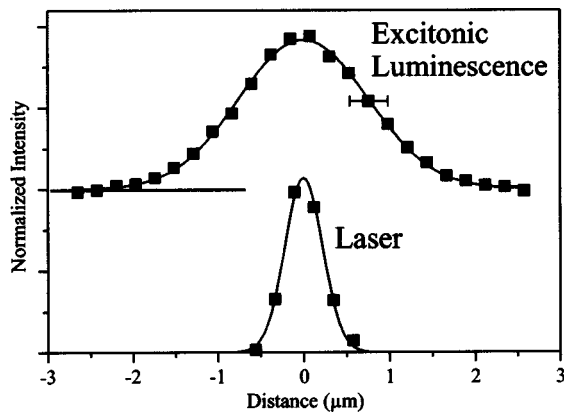


FIG. 7. Spatial profile of the excitonic luminescence of a ZnSe/ZnSSe multiple quantum well (MQW) (upper) and the corresponding excitation laser spot (lower).

to the spatial distributions of the exciton density. The field of view of the SIL²⁰ (35 μm in our setup) is far beyond the typical transport length of excitons. Figure 7 shows an example of the spatial profiles of the luminescence intensity measured for a ZnSe/ZnSSe multiple quantum well at 6 K. The excitation laser used for this measurement is a tunable cw Ti:sapphire laser pumped by an Ar-ion laser and frequency doubled using a BBO crystal. Compared to the profile of the laser excitation spot measured during the same pinhole scan, the spatial distribution of the luminescence is significantly wider due to the exciton in-plane transport. The improved resolution enables us to access the coherent transport²¹ and hot-exciton transport regimes.^{22,23}

This kind of direct transport measurement can also be performed with time resolution by using a pulsed Ti:sapphire laser, a synchroscan streak camera, and a CCD in photon-counting mode. In this configuration, one can detect the temporal evolution of the spatial profile of luminescence, as shown in Fig. 8 for a ZnSe/ZnMgSSe multiple QW. The combination of the 200 nm spatial resolution with the 2 ps temporal resolution enables one to investigate directly the energy relaxation during the exciton transport.²⁴ We note that for the time-resolved measurements, the high collection efficiency introduced by the SIL is particularly crucial not only because of the signal losses at the pinhole but also because the signal intensity is spread due to the time resolution. So, in contrast to nonlinear optical experiments with high spatial resolution, these studies can be performed in the low excitation regime where many-body interactions are negligible.

B. Single quantum dot spectroscopy

Investigation of the properties of individual quantum dots requires single dot spectroscopy. This can be achieved by reducing the number of dots (selected, e.g., by a nano-aperture or a mesa) or high spatial resolution (e.g., SNOM). In SIL-enhanced nano-PL, single dot spectroscopy can also be achieved for samples with a low dot density. In such a system, the choice of dots is more flexible. One can address a large number of individual dots and thus judge whether the

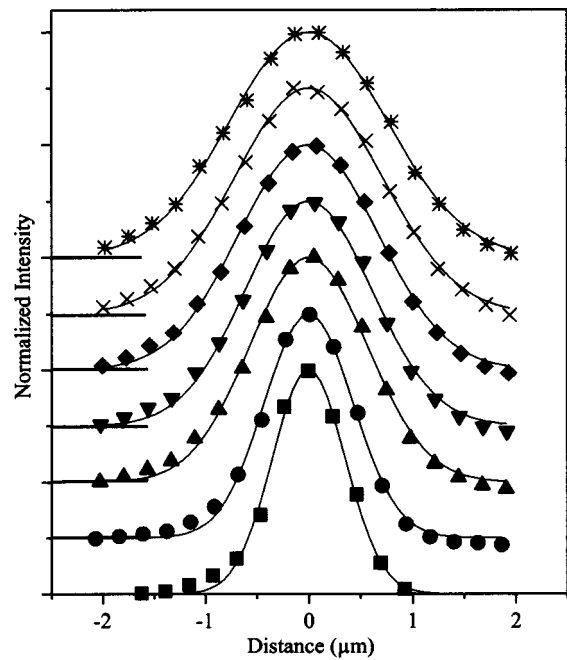


FIG. 8. Time evolution of the spatial profile of the exciton luminescence. The ZnSe/ZnMgSSe MQW sample is excited by a 150 fs laser pulse. The delay times for the curves are (from bottom to top) 43, 64, 100, 180, 260, 340, and 420 ps.

observed single-dot properties are typical for the whole ensemble. Since there is no patterning required, it is a nondestructive method.

The high spatial and spectral resolutions of the SIL-enhanced nano-PL system enable us to detect isolated narrow lines from a single quantum dot undisturbed by the luminescence from other dots. The high collection efficiency makes it an ideal system for weak-signal detection. For example, under low-density excitation the spectrum of sharp lines can still be measured with a reasonable integration time at high temperatures up to 120 K. Figure 9(a) shows a spectrum of a GaAs/AlAs superlattice. In these kinds of samples, quantum dots are formed due to interface fluctuations.²⁵ A He-Ne laser is used for excitation with an intensity of 0.5 W/cm². By introducing the SIL and the 20 μm pinhole, a large number of isolated sharp lines from individual quantum dots are well resolved. This allows us to measure accurately the temperature dependence of the homogeneous linewidth, thus study the exciton-phonon interactions in these kinds of structures.²⁶ With this setup, isolated sharp lines can also be observed for a ZnCdSe/ZnSe quantum-dot sample with a rather high dot density. In Fig. 9(b), we plot a small part of the spectrum which has been shown as Fig. 4(c) (within the dashed box) for a close-up of the well-separated lines. This enables us to study the spectral line shape of the individual lines. Increasing the sample temperature we observe a strong deviation from the Lorentzian line shape. Figure 9(c) shows one example of the line shape measured at 60 K. The observed deviation is consistent with previous results obtained on similar structures, and can be attributed to the strong coupling regime of excitonic states to acoustic phonons.²⁷ We note that with this setup, we are able to study a rather large number of the lines simultaneously. We do find that this kind

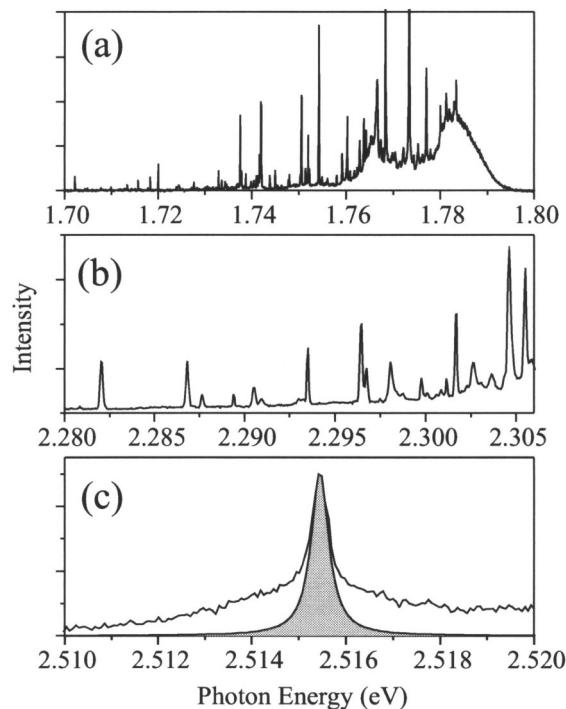


FIG. 9. Single dot spectroscopy achieved by SIL-enhanced nano-PL setup. (a) A spectrum of a GaAs/AlAs superlattice measured at a sample temperature of 22 K. (b) A part of the spectrum of a ZnCdSe/ZnSe quantum-dot sample, as shown in the dashed box of Fig. 4(c). (c) Details of an individual sharp line of the ZnCdSe/ZnSe quantum-dot sample measured at a sample temperature of 60 K. The shaded area shows a Lorentzian fit to the central part of the peak.

of deviation is a general feature of all the measured lines.²⁸

Furthermore, we confirm that the polarization information of the luminescence, which is of crucial importance, e.g., in the investigations of spin dynamics, is preserved in this setup. Figure 10 shows the spectra of a single quantum dot in a quantum well of 6.5 ML ZnCdTe embedded in ZnTe barriers. The sample is excited with the 488 nm line from an Ar-ion laser. To determine the polarization of luminescence, a linear polarizer is placed in the detection path. The spectra show a doublet structure composed of two lines which are linearly polarized along two orthogonal directions. Such line

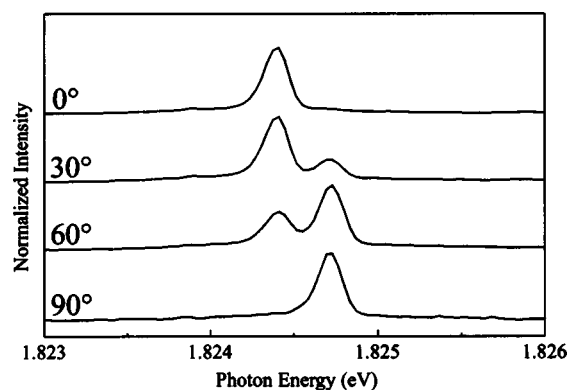


FIG. 10. SIL-enhanced nano-PL spectra of a single ZnCdTe quantum dot embedded in a ZnTe matrix as function of the angle of a linear polarizer in the detection path.

doublets are ascribed to fine-structure splitting of excitons in asymmetric quantum dots.²⁹ Our measurement demonstrates that SIL can be applied to nano-PL when the polarization of the light is of interest. It is typically very difficult to extract the polarization information from other spatially resolved techniques like near-field spectroscopy.³⁰

V. SUMMARY

We demonstrate a far-field nano-PL setup based on the combination of an h-SIL with a confocal microscope. Two advantages introduced by the SIL, an improved resolution of 0.4λ and a factor of 5 enhancement of the collection efficiency, make it an ideal system for spatially resolved spectroscopy applications. We analyze the improvement of the resolution achieved by using a pinhole in the image plane of the microscope, and determine the optimal pinhole size. The influence of the air gap between the SIL and the sample surface is investigated in detail. We confirm the tolerance of the setup to an air gap of several micrometers. Such a system is proven to be particularly suitable for the studies of exciton transport, both time integrated and time resolved, and the spectroscopy of single quantum dots with emphases on polarization dependence and low-signal detection.

ACKNOWLEDGMENTS

The author gratefully acknowledge the growth of excellent samples by the groups of M. Heuken (Aachen), of D. Hommel (Bremen), of C. Klingshirn (Karlsruhe), and of K. Ploog (Berlin). The author gratefully acknowledge P. R. Hemmer (Texas A&M University) for his critical reading and suggestions on the manuscript. This work was supported by the Deutsche Forschungsgemeinschaft.

- ¹A. Gustafsson, M.-E. Pistol, L. Montelius, and L. Samuelson, *J. Appl. Phys.* **84**, 1715 (1998).
- ²S. M. Mansfield and G. S. Kino, *Appl. Phys. Lett.* **57**, 2615 (1990).
- ³B. D. Terris, H. J. Mamin, D. Rugar, W. R. Studenmund, and G. S. Kino, *Appl. Phys. Lett.* **65**, 388 (1994).
- ⁴M. Vollmer, H. Giessen, W. Stolz, W. W. Rühle, L. Ghislain, and V. Elings, *Appl. Phys. Lett.* **74**, 1791 (1999).
- ⁵M. Vollmer, H. Giessen, W. Stolz, W. W. Rühle, A. Knorr, S. W. Kock, L. Ghislain, and V. Elings, *J. Microsc.* **194**, 523 (1999).
- ⁶M. Born and E. Wolf, *Principles of Optics* (Pergamon, Oxford, 1970).
- ⁷T. Sasaki, M. Baba, M. Yoshita, and H. Akiyama, *Jpn. J. Appl. Phys., Part 2* **36**, L962 (1997).
- ⁸M. Yoshita, T. Sasaki, M. Baba, and H. Akiyama, *Appl. Phys. Lett.* **73**, 635 (1998).
- ⁹M. Yoshita, M. Baba, S. Koshiba, H. Sakaki, and H. Akiyama, *Appl. Phys. Lett.* **73**, 2965 (1998).
- ¹⁰Q. Wu, R. D. Grober, D. Gammon, and D. S. Katzer, *Phys. Rev. Lett.* **83**, 2652 (1999).
- ¹¹Q. Wu, R. D. Grober, D. Gammon, and D. S. Katzer, *Phys. Status Solidi B* **221**, 505 (2000).
- ¹²B. Richards and E. Wolf, *Proc. R. Soc. London, Ser. A* **253**, 358 (1959).
- ¹³R. H. Webb, *Rep. Prog. Phys.* **59**, 427 (1996).
- ¹⁴G. von Freymann, D. Lürßen, C. Rabenstein, M. Mikolajczyk, H. Richter, H. Kalt, T. Schimmel, M. Wegener, K. Okhawa, and D. Hommel, *Appl. Phys. Lett.* **76**, 203 (2000).
- ¹⁵K. Koyama, M. Yoshita, M. Baba, T. Tohru, and H. Akiyama, *Appl. Phys. Lett.* **75**, 1667 (1999).
- ¹⁶M. Yoshita, K. Koyama, M. Baba, and H. Akiyama, *J. Appl. Phys.* **92**, 862 (2002).
- ¹⁷M. Yoshita, K. Koyama, Y. Hayamizu, M. Baba, and H. Akiyama, *Jpn. J. Appl. Phys., Part 2* **41**, L858 (2002).

- ¹⁸V. Zwiller and G. Björk, *J. Appl. Phys.* **92**, 660 (2002).
- ¹⁹M. Baba, T. Sasaki, M. Yoshita, and H. Akiyama, *J. Appl. Phys.* **85**, 6923 (1999).
- ²⁰G. S. Kino, in *Optical Pulse and Beam Propagation*, edited by Y. B. Band (SPIE, Washington, 1999), Proc. SPIE **3609**, 56 (1999).
- ²¹H. Zhao, S. Moehl, and H. Kalt, *Phys. Rev. Lett.* **89**, 097401 (2002).
- ²²H. Zhao, S. Moehl, S. Wachter, and H. Kalt, *Appl. Phys. Lett.* **80**, 1391 (2002).
- ²³H. Zhao, S. Moehl, and H. Kalt, *Appl. Phys. Lett.* **81**, 2794 (2002).
- ²⁴H. Zhao, B. Dal Don, S. Moehl, and H. Kalt, *Phys. Rev. B* **67**, 035306 (2003).
- ²⁵D. Gammon, E. S. Snow, B. V. Shanabrook, D. S. Katzer, and D. Park, *Science* **273**, 87 (1996).
- ²⁶H. Zhao, S. Wachter, and H. Kalt, *Phys. Rev. B* **66**, 085337 (2002).
- ²⁷L. Besombes, K. Kheng, L. Marsal, and H. Mariette, *Phys. Rev. B* **63**, 144307 (2001).
- ²⁸B. Dal Don, H. Zhao, S. Moehl, C. Ziegler, and H. Kalt, *Phys. Status Solidi C* (to be published).
- ²⁹L. Besombes, L. Marsal, K. Kheng, T. Charvolin, L. S. Dang, A. Wasiela, and H. Mariette, *J. Cryst. Growth* **214/215**, 742 (2000).
- ³⁰G. Eggers, A. Rosenberger, N. Held, G. Güntherodt, and P. Fumagalli, *Appl. Phys. Lett.* **79**, 3929 (2001).